

In situ observation of mechanical damage within a SiC-SiC ceramic matrix composite

L. Saucedo-Mora^{1,2}, T. Lowe³, S. Zhao², P.D. Lee⁴, P.M. Mummery⁵ and T.J. Marrow²

1. Institute Eduardo Torroja for Construction Sciences-CSIC, Madrid, Spain
2. Department of Materials, University of Oxford, UK
3. Manchester X-ray Imaging Facility, The University of Manchester, UK
4. Research Complex at Harwell, Rutherford Appleton Laboratory, UK
5. School of Mechanical, Aerospace and Civil Engineering, The University of Manchester, UK

Abstract

SiC-SiC ceramic matrix composites are candidate materials for fuel cladding in Generation IV nuclear fission reactors and as accident tolerant fuel clad in current generation plant. Experimental methods are needed that can detect and quantify the development of mechanical damage, to support modelling and qualification tests for these critical components. In situ observations of damage development have been obtained of tensile and C-ring mechanical test specimens of a braided nuclear grade SiC-SiC ceramic composite tube, using a combination of ex situ and in situ computed X-ray tomography observation and digital volume correlation analysis. The gradual development of damage by matrix cracking and also the influence of non-uniform loading are examined.

1 Introduction

Due to their high temperature capability and damage tolerance, SiC-SiC_{fibre} ceramic matrix composites are candidate materials for fuel cladding in Generation IV nuclear fission reactor concepts such as the gas cooled fast reactor (GFR) [1]. They have also been proposed for accident-tolerant fuel cladding for current (Gen II/III) light water reactors (LWR) [2] and as structural materials in some designs of the tritium-breeding 'blanket' for nuclear fusion power generation [3]. All of these components must operate safely at temperatures far exceeding current heat-resistant metallic alloy capabilities. To fabricate these composites, the material choice is restricted exclusively to nuclear grade constituents that have the essential pre-requisite of neutronic compatibility [4–6] (e.g. 3rd generation stoichiometric and highly crystalline SiC fibres, a pyrolytic carbon interphase and a β -SiC matrix formed by chemical vapour infiltration); these materials are thermally stable and retain their strength and toughness to temperatures above 1600°C.

Nuclear grade SiC-SiC_{fibre} composite development has largely taken place within the international fusion materials' programmes, fabricated and investigated as flat panels or plates to optimize the microstructure for thermo-mechanical properties; unidirectional fibres or 2-dimensional satin-weaves have typically been studied. More recently, within the European nuclear fission programme, a tubular pin-type GFR fuel clad geometry with filament wound or braided architectures has been designed [1], whilst for accident tolerant LWR fuel clad, layered monolithic SiC and SiC-SiC_{fibre} composite structures have been proposed [7]. Component testing is critical for composites, since the act of assembling specific clad shapes into components affects the microstructure. It is necessary to optimize their fabrication; for instance, to determine whether filament winding or lower-cost braiding is optimal for the different layers in tubular components. Ultimately, testing in realistic conditions of fast neutron flux and temperature will be essential to evaluate fully these structures. Macroscopic mechanical tests (e.g. [8]) provide an assessment of the average properties of the composite, and are crucial data for design. Such tests may be used also to evaluate the effects of irradiation and oxidation, batch-batch variations in properties and also the sensitivity to composite fabrication; different composite weaves will develop different patterns of stress in the matrix [9], and heterogeneities in the weave will be responsible for variations in the onset of matrix damage and interface failures [10,11]. Component tests will be critical also to evaluate the complex structures of joints [12].

Given the importance of microstructure damage to the mechanical and thermal characteristics of these composites, reliable methods to assess its development are essential. The aim of this work was therefore to investigate whether the combined use of X-ray computed tomography and image correlation could detect and quantify damage during the in situ testing of ceramic matrix composites. The work was performed as part of Work Package 3 of the MatISse Collaborative Project "Materials' Innovations for Safe and Sustainable Nuclear" (European Commission Seventh Framework Programme), which supports the European Energy Research Alliance Joint Programme on Nuclear Materials [13]. A key objective was to be able to investigate how damage develops in a structural component of representative size, under a known state of loading. Such data may

This is the author's copy of a paper that was subsequently published in Journal of Nuclear Materials 481 (2016) pp13-23, <http://dx.doi.org/10.1016/j.jnucmat.2016.09.007>

ultimately be used to validate numerical models (e.g. [14]) to support the prediction of mechanical performance under different states of loading.

2 Experimental

2.1 Material

The SiC-SiC material, provided by the MatISse consortium [13], was fabricated from nuclear grade constituents by CEA (French Alternative Energies and Atomic Energy Commission) [15]. The ceramic composite tubes were produced by CVI onto the fibre preform in the same manner as described in ref. [16]; they comprised an inner SiC fibre filament wound layer ($\pm 45^\circ$) with two-layers of 2-dimensional braided structure ($\pm 45^\circ$). The inner and outer surfaces had been mechanically ground. The inner and outer diameters are 7.80 and 9.75 mm respectively. Cutting of the test specimens from these tubes was done at the University of Oxford, using a 1 mm width diamond circular saw with a water-based coolant applied during the cut.

To characterise the microstructure, a length of the composite tube was examined by synchrotron X-ray computed tomography on the I12 Joint Engineering, Environment and Processing (JEEP) beam line at the UK Diamond Light Source. A series of adjacent observations were obtained at a voxel size of 3.25 μm with 56 keV X-ray energy, each with a volumetric field of view of 8.3 x 8.3 x 7 mm. Each tomograph was produced from 1800 radiographs collected over 180° rotation. Due to the sample diameter and its position in the smaller field of view, half of the tube's cross-section was imaged over a length of 24 mm; the total material volume characterised was $\sim 340 \text{ mm}^3$. The duration of each scan was approximately 10 minutes. A length of tube was also scanned by high-resolution computed X-ray tomography using an Xradia Versa 500 X-ray microscope at 80 keV X-ray energy at the Manchester X-ray Imaging Facility. Three overlapping tomographs of the tube wall were obtained at different heights along the tube axis, each with a volumetric field of view of 3.5 x 3.5 x 3.5 mm and a voxel size of 1.7 μm . Each tomograph was produced from 1991 radiographs collected over 360° rotation. The overlap between the scans was 0.5 mm; the total material volume characterised was 21.4 mm^3 . The duration of each scan was approximately 6.5 hours.

2.2 Mechanical Testing

2.2.1 Axial Tensile Test

A length of the composite tube was tested in tension, using a loading stage mounted on a laboratory tomography microscope. The loading stage (Deben with 20 kN load cell) is described in more detail in reference [17]. The tomographs were obtained using a Nikon Custom Bay X-ray Microscope at the Manchester X-ray Imaging Facility; the specimen was mounted with a flexible coupling to allow axial tensile loading (Figure 1a). Each end of the specimen was bonded by a cold-setting epoxy resin within a cylindrical hole (depth 10 mm, diameter 13 mm), with a free length of 35 mm (total specimen length 55 mm). This setup permitted medium resolution computed tomography scans with a voxel size of 17 μm at a volumetric field of view of 34 x 34 x 34 mm. The volume of material characterised was ~ 960

This is the author's copy of a paper that was subsequently published in Journal of Nuclear Materials 481 (2016) pp13-23, <http://dx.doi.org/10.1016/j.jnucmat.2016.09.007>

mm³ and the beam energy was 80 keV. Each tomograph was produced from 3144 radiographs collected over 180° rotation with a duration of approximately 3 hours.

After a reference scan in the unloaded state, the tube sample was mechanically loaded in tension in displacement control to 400 N and scanned again. It was then unloaded to 20 N; scanned; reloaded to 800 N; scanned; unloaded to 20 N; scanned; then reloaded to 1200 N. An equipment failure (burnt-out filament in the X ray source) prevented the scan from being completed at 1200 N. The peak loads correspond to axial tensile stresses of 17.3 MPa, 34.6 MPa and 52.0 MPa. The specimen was then transferred to an Xradia Versa 500 X-ray microscope at the same facility. Tomographs of the tube wall were obtained, at 80 keV X-ray energy, at different heights along the tube axis, each with a volumetric field of view of 3.5 x 3.5 x 3.5 mm and a voxel size of 1.7 µm. The specimen was not loaded during these observations.

2.2.2 C-ring Diametral Test

A 'C-ring' specimen (Figure 1b) was loaded within the same University of Manchester Deben rig (2 kN load cell) while observed using synchrotron X-ray computed tomography on the Joint Engineering, Environment and Processing (JEEP) beamline I12 at the Diamond Light Source. The specimen width was 4 mm. Compression along the specimen's vertical diameter produced a tensile strain on the outer surface that was sufficient to cause fracture as the load was increased under displacement control in steps to ~120 N. These synchrotron X-ray tomography observations were obtained at a voxel size of 3.25 µm and a volumetric field of view of 8.3 x 8.3 x 7 mm, with 56 keV X-ray energy. Observations were obtained under load at each step, and also when unloaded to approximately 5 N between steps. Each tomograph was produced from 1800 radiographs collected over a 180° rotation.

Following the C-ring test, the damaged specimen was examined, unloaded, using a North Star Instruments X5000 computed tomography instrument at 60 keV X-ray energy; the voxel size was 3.5 µm and the duration of this scan was approximately 2 hours. The same specimen was also examined, without load, using a Zeiss Xradia Versa 520 at the Hans Mahl Nanosolution Center (Germany) with 60 keV X-ray energy; the voxel size was 1 µm, the volumetric field of view was 1 x 1 x 1 mm and the characterised volume of material was ~0.8 mm³. The tomograph was produced from 3001 radiographs collected over 360° rotation and the duration of this scan was approximately 10 hours.

3 Results

3.1 Microstructure and Damage Characterisation

The structure of the composite tube is visualised in Figure 2a and b using the medium-resolution (17.5 µm voxel) laboratory tomography data. A cross-section of the microstructure (Figure 2c and d), obtained by laboratory tomography at 1.75 µm voxel resolution, shows the finer-scale structure of the composite, in which the filament wound layer and braided fibre tows can be identified. Segmentation of the porosity via image intensity thresholding was done using the Avizo Fire software (Figure 2e). The contrast between pores and solid material is sufficiently high that the quantitative analysis is

This is the author's copy of a paper that was subsequently published in Journal of Nuclear Materials 481 (2016) pp13-23, <http://dx.doi.org/10.1016/j.jnucmat.2016.09.007>

insensitive to the chosen segmentation thresholds. The analysis of the segmented pores shows that tomographs at different resolutions captured an equivalent total porosity (Figure 3a). The average porosity content, measured within segments of 0.015 mm length, varies along the tube section and similar data for the average porosity (~5 to 7%) are obtained in medium resolution (17 μm voxel) and high resolution (3.25 μm voxel) tomography scans that studied different tubes. The smallest pores, which make up a small fraction of the total porosity, are best characterised at higher resolution (Figure 3b); the lowest resolution tomographs examined a sufficiently large volume to observe the largest pores in the population, which are up to 1 mm in size when measured in the tangential direction of each layer of the tube.

It is not possible to resolve any microstructure damage in the tensile tested tube in the tomographs at 17.5 μm and 1.75 μm voxel size. However, the unloaded C-ring, visualised with 3.5 μm tomography in Figure 4a after being mechanically tested to failure, clearly shows the development of damage. Cracking and spalling of the monolithic SiC layer has occurred, exposing the SiC fibres. The cracks then propagated from the concave surface inwards through the SiC matrix, and were deflected by the fibre tows (Figure 4b). The higher resolution observations (at 1 μm voxel) at the same location (Figure 4c) confirm the absence of fibres in outer layer, and also show that in the main body of the composite the crack propagated predominantly between the fibres. Some broken fibres are also found. These appear with greater frequency close to the monolithic layer (Figure 4d), and some may have originated from mechanical damage during the surface grinding, but broken fibres are also observed deeper in the specimen. These are shown in the tomograph sections in Figure 4e, which are aligned parallel and perpendicular to the fibre tows.

3.2 Digital Volume Correlation Analysis

3.2.1 Axial Tensile Test

Digital volume correlation (DVC) analysis, to measure the three-dimensional full field displacements between successive tomographs, was applied to the medium resolution (17 μm) tomographs of the tensile tested composite tube. The analysis used the LaVision Davis software. The reference tomograph was the initial unloaded specimen. An anisotropic interrogation subset was used due to the small number of voxels across the wall thickness (~50 voxels) at this resolution. The subset size was 128 x 128 x 256 voxels, with the elongated dimension of the subset aligned parallel to the tube axis; the overlap of subsets was 75% with 2 passes performed.

Examples of the obtained displacement fields for the tube under load at 400 N and 800 N are shown in Figure 5; the displacement vectors in the horizontal plane are presented (relative to the average displacement of the tube, and magnified by several orders of magnitude), together with the magnitude of the maximum principal strain. Rigid body movements in the DVC data, relative to the average displacement of the data, have been removed. The deformation is quite uniform at 400 N, except at the 25 mm height close to the upper fixture, but as the load increased the composite tube begins to deform non-uniformly and this deformation is not recovered when the load is removed.

This is the author's copy of a paper that was subsequently published in Journal of Nuclear Materials 481 (2016) pp13-23, <http://dx.doi.org/10.1016/j.jnucmat.2016.09.007>

Three-dimensional visualisations of the maximum principal strain, both under load and after unloading, are shown in Figure 6. These show the progressive development of localised strains that are distributed non-uniformly throughout the sample. The magnitudes of the strains decrease on unloading, but the pattern of strains remains. There is a greater degree of deformation towards the upper end of the tube.

It was not possible to apply extensometers or strain gauges in the tomography experiments due to the requirements of sample rotation during scans and also the dimensional constraints of the loading rig. However, the displacement fields measured by DVC provide information that can be used to investigate the tensile elongation of the tube sample. The relative axial displacements around the tensile loaded tube circumference were measured between positions that were separated by a vertical distance of 8.2 mm; the location of this gauge length between the approximate heights of $z=7$ mm and $z=15$ mm is shown in Figure 6. The estimated error in individual displacement magnitude measurements by DVC is approximately 0.5 voxel (i.e. 8.5 μm). This is based on previous studies that applied DVC to similar quality tomographs [18], as it was not possible to obtain a measurement of this due to the limited number of scans that could be performed in the tensile experiment. The estimated uncertainty in the average tensile strain, calculated from displacement measurements separated by the 8.2 mm gauge length, is 0.15%.

Example data at 800 N are shown in Figure 7a for the movements of the top and bottom of the gauge length. The deformation is quite non-uniform, and is concentrated to one side of the tube. In terms of average strain across the gauge length (Figure 7b), there are regions of tension and compression that are separated by approximate 90° intervals around the circumference. This strain is not fully recovered on unloading. This is shown more clearly in Figure 8, in maps of the local axial strains within the selected 8.2 mm gauge length around the circumference of the tube. The magnitude of the local strains increases with applied load, and the same pattern is maintained after unloading, indicating localised deformation that is not recovered.

3.2.2 C-ring Diametral Test

DVC analysis was also applied to measure the three-dimensional full field displacements between the successive high-resolution synchrotron X-ray tomographs (at 3.25 μm voxel) of the diametrically loaded C-ring specimen. The reference tomograph was the initial unloaded specimen. The DVC analysis of loaded and unloaded tomographs was done with a subset size of 128 x 128 x 128 voxels at 50% overlap. An analysis of tomographs between which the unloaded specimen was physically translated by 50 μm has a standard deviation of the displacement vector magnitude of 1.2 μm . This was regarded as the measurement uncertainty (i.e. approximately 0.4 voxel), and is typical for DVC of tomographs [18].

In the tested C-ring specimen, a heterogeneous distribution of localised strains is observed, which develops progressively in magnitude and extent with increasing applied load (Figure 9a). Localised strains remain, with reduced magnitude, after the load is removed (Figure 9b). The strains are not uniformly distributed, appear initially in the upper part of the sample and span the sample width. The strains are superposed on tomography slices of the damaged sample in Figure 10, which shows that regions of high tensile strain correspond to

This is the author's copy of a paper that was subsequently published in Journal of Nuclear Materials 481 (2016) pp13-23, <http://dx.doi.org/10.1016/j.jnucmat.2016.09.007>

observable cracks. These cracks are just visible in the tomographs whilst the specimen is under load (Figure 10a), but cannot be resolved readily by tomographic imaging when the specimen is unloaded (Figure 10b), unless significant damage has developed (Figure 4).

The bulk deformation of the C-ring was investigated using the displacement field that was obtained via the DVC analysis. The compressive displacement change relative to the initial state was measured across a vertical gauge distance of 5.4 mm (Figure 11a). The gauge distance was centred about the middle of the sample. The average displacements over the full 4 mm width and 1 mm thickness of the sample were used; the error bars represent their standard deviations. This gauge length of the specimen rotated by less than 12° about a horizontal axis during the experiment, and the vertical displacement data have not been corrected to remove this small effect. The displacement change increases with applied load, and there is a small increase, with increasing peak load, of the residual compressive displacement change that is observed after unloading. The average compliance across this vertical gauge length was obtained during both loading and unloading in each cycle (Figure 11b). There is a progressive increase in compliance up to a peak load of about 100 N – above this the data become unreliable as the deformation of the specimen was non-uniform. Very similar compliance values are obtained from the loading and unloading data.

4 Discussion

The expected structural design criterion for SiC-SiC_{fibre} composites will be some fraction of the proportional limit stress (PLS) [19]. This is the critical stress, in tensile loading, above which non-linear stress/strain behaviour is observed, and it is known to be associated with the development of significant matrix cracking [16]; further cracking develops as the applied strain increases. The propagation of cracks is resisted by the ‘fibre pull out’ toughening mechanism from the continuous, high strength SiC fibres, and this governs the component’s strength [20,21]. Microcracking of the matrix also affects the heat transfer properties of the ceramic composite fuel cladding [22].

In a comprehensive study of the effects of stress state on the strength and stiffness of SiC-SiC ceramic matrix composite tubes [16], acoustic emission and surface observations augmented by digital image correlation analysis were used to characterise the development of matrix cracking. The composite was fabricated from layers of filament wound and braided tows of Hi-Nicalon type S fibres, with a pyrocarbon interphase applied to the fibre preform before the SiC matrix was introduced via Chemical Vapour Infiltration (CVI). Matrix cracking, which saturated rapidly at approximately at a density of 2 mm⁻¹, was associated with acoustic emission and the onset of non-linear mechanical behaviour. In tensile loading, this occurred at applied strains above approximately 0.04%.

In situ observations by computed X-ray tomography during tensile tests of a single tow of a SiC-SiC composite [23] have shown that the surface observations do not fully characterise damage development. The material studied was a single tow of 500 Hi-Nicalon type S fibers, coated a pyrocarbon interphase with a CVI-deposited SiC matrix. The tomography observations, obtained only when the applied strain above 0.15%, showed that the density of matrix cracks increased with applied strain and saturated at a higher density of about 4

This is the author’s copy of a paper that was subsequently published in Journal of Nuclear Materials 481 (2016) pp13-23, <http://dx.doi.org/10.1016/j.jnucmat.2016.09.007>

mm⁻¹. These major cracks led to fibre failure, although minor cracking was also observed. Similar behaviour was observed in computed X-ray tomography observations at 1750°C [24] of a tensile test of a single tow of 500 Nicolon-S fibres with a CVI-deposited SiC matrix. Matrix cracking extended until the load was taken fully by the intact fibres. Ex-situ studies of larger samples fabricated from the same materials that were tested at room temperature developed a saturated matrix crack density of 2 mm⁻¹, similar to that observed in other studies, e.g. [16]. It is thus important to recognise the role the composite meso-scale structure may have on damage development, as this will affect the local strains in matrix and fibres in response to the macroscopic applied strains.

The analysis of the observed porosity (Figure 3) demonstrates that computed X-ray tomography can provide an effective quantitative assessment of pores that are sufficiently large; pores need to be at least an order of magnitude larger than the voxel size to be measured reliably. The large pores at the meso-scale provide the bulk of the total porosity, which was between 5 and 7% of the sample volume. This is lower than detected by Bernachy [16] for similarly fabricated composites; the average porosity measured in three samples using X-ray tomography was reported to be between 10.4% and 11.1%, although the voxel resolution in that work is not stated, and characterisation of voids in tomographs can be sensitive to segmentation methods [25]. The reproducibility at different resolution of the measurements (Figure 3) of the larger voids gives confidence in these data. At a pore size of about 200 µm, there is a change in gradient of the power-law relationship that is observed between pore size and number density. This may describe different pore populations within and between the fibre tows in the braided structure. The large pores between the fibre tows are significant to damage development, as observed in Figure 10, and their size and distribution may be affected by differences in manufacturing.

Digital volume correlation of tomographs can measure the three-dimensional deformation behaviour in response to applied loads, and can also be used to detect cracking as shown by the comparison of the strain maps and tomographs (Figure 10). The observed strains are due to permanent damage; the opening displacements of cracks are visualised as strain, and these relax when the load is removed. The measured local strains (e.g. Figure 6 and Figure 9) are not real strains of the material, but arise from the effect of crack openings on local gradients between discrete measurements in the displacement field. The residual strains indicate that some permanent deformation has occurred, such that the unloaded cracks do not fully close. This may be due to the “textile effect” that has been attributed to the reorientation of fibre tows under load in damaged microstructures [16]. It is interesting to note that regions of tensile strain exist on the inner surface of the C-ring specimen after unloading (Figure 10b); this part of the specimen would have been under compression during loading and develops an array of cracks once unloaded, with an average separation of approximately 0.5 mm (i.e. ~2 mm⁻¹). The density of cracking is of a similar magnitude to that reported previously [16,23]. It is also interesting to note the difference in cracking behaviour between the monolithic SiC layer and the braided microstructure (Figure 4). Surface observations of cracking [11,16] might not be fully representative of sub-surface damage in the composite structure, although it is clear from the C-ring test that surface cracks may act as initiation sites (Figure 4).

The tensile stress strain behaviour of similar composite tubes tested by Bernachy [16] exhibited significant non-linearity for applied tensile stresses above 125 MPa. The onset of non-linearity corresponded to the onset of significant microcracking damage, which was detected by acoustic emission. The change in compliance of the C-ring specimen in this work is also consistent with progressive accumulation of cracking damage in the specimen (Figure 4), with negligible inelastic deformation. The elastic modulus is reduced by the presence of multiple cracks. The increase in the residual displacement in the unloaded state (Figure 11) may be simply be due to the high elastic compliance after significant damage has been introduced, as a nominal load of 5 N was applied during these observations.

In the tensile loading of the composite tube in this work, the equivalent applied tensile stresses at 400 N and 800 N are approximately 17.5 MPa and 35 MPa respectively. These are substantially lower than the tensile stress at which significant microcracking would be expected, but the localised strains indicate that cracking damage is developing. The deformation develops non-uniformly at the macro-scale (Figure 5) and also at the meso-scale (Figure 7). The measured deformation initially appears quite uniform at 400 N (Figure 5a and Figure 8a) except close to the upper fixture. The fixtures of the jig allowed movement of the specimen to facilitate alignment of the load with its axis (Figure 1a), but constraint near the fixtures of the specimen may affect the deformation. The magnitudes of the measured average strains across the selected 8.2 mm gauge length (Figure 7b) are of the order of those that caused micro-cracking damage in similar composites [16,23]. The precision of displacement measurement by DVC of tomographs at this resolution is not very high, however, and some experimental misalignment cannot be ruled out, such that the assumed tensile stresses may be inaccurate. Hence, the non-uniform pattern of damage observed in the tensile test is likely to be due to an initial misalignment of the loading applied to the specimen. The non-uniformity of the measured deformation of the tensile test increases as the load increases. This suggests that the development of damage affects the compliance and the resulting distribution of strain. Spatial variations of the stiffness change the distribution of stress and the consequent deformation and development of further damage. For instance, at 800 N tensile load, the tensile deformation has become concentrated on one side of the tube (Figure 7a). The braided microstructure may also introduce further heterogeneity of mechanical properties at the meso-scale, which appears in the patterns of deformation caused by damage (Figure 7b).

In summary, combined application of digital volume correlation with in situ X-ray tomography of loaded test specimens provides a tool to measure the applied deformation and to detect the locations of damage, which are shown by high resolution ex-situ observations to be due to cracking of the SiC matrix. Such observations might later be coupled with thermal property measurements (e.g. [22]), to better understand the effects of mechanical damage on the thermal performance of ceramics for nuclear fuel clad. In principal, these methods could also be applied under conditions of high temperature and multi-axial or internal pressure loading that more closely simulate the operating or screening test environments.

5 Conclusion

The feasibility has been demonstrated of in situ observation of damage development during mechanical testing of the ceramic composite component, using a combination of computed X-ray tomography and digital volume correlation analysis. The large pores between the fibre tows are significant to damage development, and computed X-ray tomography can provide an effective quantitative assessment of these; smaller pores that are not sufficiently large relative to the voxel size are not measured reliably. Digital volume correlation of the tomographs can measure the three-dimensional deformation behaviour in response to applied loads, detecting cracking and observing residual that may be due to a “textile effect” attributed to the reorientation of fibre tows under load in damaged microstructures.

6 Acknowledgements

This study was carried out within the UK Engineering and Physical Sciences Research Council (EPSRC) project “QUBE: Quasi-Brittle fracture: a 3D Experimentally-validated approach” (EP/J019992/1), which supported LS-M and TJM. The support of TJM by the Oxford Martin School at the University of Oxford is also gratefully acknowledged. Additional support was also obtained for LS-M from the EPSRC Characterisation of Nanomaterials for Energy Platform Grant at Oxford University (EP/K032518/1). Access to the UK Diamond Light Source was provided via Experiment EE10106, and the assistance provided by Dr Christina Reinhard is appreciated. We acknowledge funding from the UK EPSRC for the Manchester X-ray imaging facility, which was funded in part by EPSRC grants EP/F007906/1, EP/F001452/1 and EP/I02249X/1. We are grateful to Dr Rosy Manser of Carl Zeiss Ltd and Dr Holger Blank of Carl Zeiss Microscopy GmbH for providing access to the Xradia Versa 520 at the Hans Mahl Nanosolution Center, and to Mr Guy Tolley and Mr Julien Noel for access to the X5000 at North Star Imaging, Paris. This work contributes to Work Package 3 of the MatISse Collaborative Project “Materials’ Innovations for Safe and Sustainable Nuclear” (European Commission Seventh Framework Programme Grant 604862, FP7-Fission-2013), which supplied the materials and also supported access to the Manchester X-ray Imaging Facility. Data can be obtained from the corresponding author.

7 References

- [1] F. Carre, P. Yvon, P. Anzieu, N. Chauvin, J.-Y. Malo, Update of the French R&D strategy on gas-cooled reactors, *Nucl. Eng. Des.* 240 (2010) 2401–2408. doi:10.1016/j.nucengdes.2010.02.042.
- [2] C. Sauder, A. Michaux, G. Loupiau, P. Billaud, J. Braun, Assessment of SiC/SiC cladding for LWRs, in: *LWR Fuel Perform. Meet. Top Fuel 2013*, American Nuclear Society, 2013: pp. 951–956.
- [3] Y. Katoh, L.L. Snead, C.H. Henager, A. Hasegawa, A. Kohyama, B. Riccardi, et al., Current status and critical issues for development of SiC composites for fusion applications, *J. Nucl. Mater.* 367-370 (2007) 659–671.

This is the author’s copy of a paper that was subsequently published in *Journal of Nuclear Materials* 481 (2016) pp13-23, <http://dx.doi.org/10.1016/j.jnucmat.2016.09.007>

doi:10.1016/j.jnucmat.2007.03.032.

- [4] G. Newsome, L.L. Snead, T. Hinoki, Y. Katoh, D. Peters, Evaluation of neutron irradiated silicon carbide and silicon carbide composites, *J. Nucl. Mater.* 371 (2007) 76–89. doi:10.1016/j.jnucmat.2007.05.007.
- [5] T. Nozawa, Y. Katoh, L.L. Snead, The effect of neutron irradiation on the fiber/matrix interphase of silicon carbide composites, *J. Nucl. Mater.* 384 (2009) 195–211. doi:10.1016/j.jnucmat.2008.11.015.
- [6] Y. Katoh, L.L. Snead, T. Nozawa, S. Kondo, J.T. Busby, Thermophysical and mechanical properties of near-stoichiometric fiber CVI SiC/SiC composites after neutron irradiation at elevated temperatures, *J. Nucl. Mater.* 403 (2010) 48–61. doi:10.1016/j.jnucmat.2010.06.002.
- [7] C.P. Deck, G.M. Jacobsen, J. Sheeder, O. Gutierrez, J. Zhang, J. Stone, et al., Characterization of SiC–SiC composites for accident tolerant fuel cladding, *J. Nucl. Mater.* 466 (2015) 667–681. doi:10.1016/j.jnucmat.2015.08.020.
- [8] G.M. Jacobsen, J.D. Stone, H.E. Khalifa, C.P. Deck, C.A. Back, Investigation of the C-ring test for measuring hoop tensile strength of nuclear grade ceramic composites, *J. Nucl. Mater.* 452 (2014) 125–132. doi:10.1016/j.jnucmat.2014.05.002.
- [9] D. Zhang, D.R. Hayhurst, Stress–strain and fracture behaviour of 0°/90° and plain weave ceramic matrix composites from tow multi-axial properties, *Int. J. Solids Struct.* 47 (2010) 2958–2969. doi:10.1016/j.ijsolstr.2010.06.023.
- [10] T. Nozawa, E. Lara-Curzio, Y. Katoh, R.J. Shinavski, Tensile properties of advanced SiC/SiC composites for nuclear control rod applications, in: *Ceram. Eng. Sci. Proc.*, 2008: pp. 223–234.
- [11] E. Rohmer, E. Martin, C. Lorrette, Mechanical properties of SiC/SiC braided tubes for fuel cladding, *J. Nucl. Mater.* 453 (2014) 16–21. doi:http://dx.doi.org/10.1016/j.jnucmat.2014.06.035.
- [12] M. Ferraris, M. Salvo, V. Casalegno, *Ceramic Integration and Joining Technologies*, John Wiley & Sons, Inc., Hoboken, NJ, USA, 2011. doi:10.1002/9781118056776.
- [13] C. Cabet, A. Michaux, C. Fazio, L. Malerba, M.F. Maday, M. Serrano, et al., The new EC FP7 MatISSE project: materials' innovations for a safe and sustainable nuclear in Europe, in: *SMINS-3, Struct. Mater. Innov. Nucl. Syst. - Work. Proceedings*, Idaho Natl. Lab. Idaho Falls, United States, 7-10 Oct. 2013, 2013.

This is the author's copy of a paper that was subsequently published in *Journal of Nuclear Materials* 481 (2016) pp13-23, <http://dx.doi.org/10.1016/j.jnucmat.2016.09.007>

- [14] L. Saucedo-Mora, T.J. Marrow, Multi-scale damage modelling in a ceramic matrix composite using a finite-element microstructure meshfree methodology, *Philos. Trans. R. Soc. London A Math. Phys. Eng. Sci.* 374 (2016). doi:10.1098/rsta.2015.0276.
- [15] C. Sauder, *Ceramic Matrix Composites: Nuclear Applications*, in: Wiley Blackwell, 2014: pp. 609–646. doi:10.1002/9781118832998.ch22.
- [16] F. Bernachy-Barbe, L. Gélébart, M. Bornert, J. Crépin, C. Sauder, Anisotropic damage behavior of SiC/SiC composite tubes: Multiaxial testing and damage characterization, *Compos. Part A Appl. Sci. Manuf.* 76 (2015) 281–288. doi:10.1016/j.compositesa.2015.04.022.
- [17] M. Mostafavi, S.A. McDonald, H. Çetinel, P.M. Mummery, T.J. Marrow, Flexural strength and defect behaviour of polygranular graphite under different states of stress, *Carbon N. Y.* 59 (2013) 325–336. doi:10.1016/j.carbon.2013.03.025.
- [18] Y. Vertyagina, M. Mostafavi, C. Reinhard, R. Atwood, T.J. Marrow, In situ quantitative three-dimensional characterisation of sub-indentation cracking in polycrystalline alumina, *J. Eur. Ceram. Soc.* 34 (2014) 3127–3232. doi:10.1016/j.jeurceramsoc.2014.04.002.
- [19] T. Nozawa, S. Kim, K. Ozawa, H. Tanigawa, Stress envelope of silicon carbide composites at elevated temperatures, *Fusion Eng. Des.* (2014). doi:10.1016/j.fusengdes.2013.12.032.
- [20] N. Lissart, J. Lamon, Damage and failure in ceramic matrix minicomposites: Experimental study and model, *Acta Mater.* 45 (1997) 1025–1044.
- [21] J. Lamon, *Ceramic Matrix Composites*, John Wiley & Sons, Inc., Hoboken, NJ, USA, 2014. doi:10.1002/9781118832998.
- [22] J. El Yagoubi, J. Lamon, J.-C. Batsale, J. Dhote, M. Le Flem, Multiscale Thermal Characterization of Mechanically Loaded Ceramic Matrix Composite, *Exp. Mech.* 55 (2015) 783–794. doi:10.1007/s11340-014-9976-x.
- [23] C. Chateau, L. Gélébart, M. Bornert, J. Crépin, E. Boller, C. Sauder, et al., In situ X-ray microtomography characterization of damage in SiCf/SiC minicomposites, *Compos. Sci. Technol.* 71 (2011) 916–924. doi:10.1016/j.compscitech.2011.02.008.
- [24] H.A. Bale, A. Haboub, A.A. MacDowell, J.R. Nasiatka, D.Y. Parkinson, B.N. Cox, et al., Real-time quantitative imaging of failure events in materials under load This is the author's copy of a paper that was subsequently published in *Journal of Nuclear Materials* 481 (2016) pp13-23, <http://dx.doi.org/10.1016/j.jnucmat.2016.09.007>

at temperatures above 1,600 °C., Nat. Mater. 12 (2013) 40–6.
doi:10.1038/nmat3497.

- [25] Y. Nikishkov, L. Airoidi, A. Makeev, Measurement of voids in composites by X-ray Computed Tomography, Compos. Sci. Technol. 89 (2013) 89–97.
doi:10.1016/j.compscitech.2013.09.019.

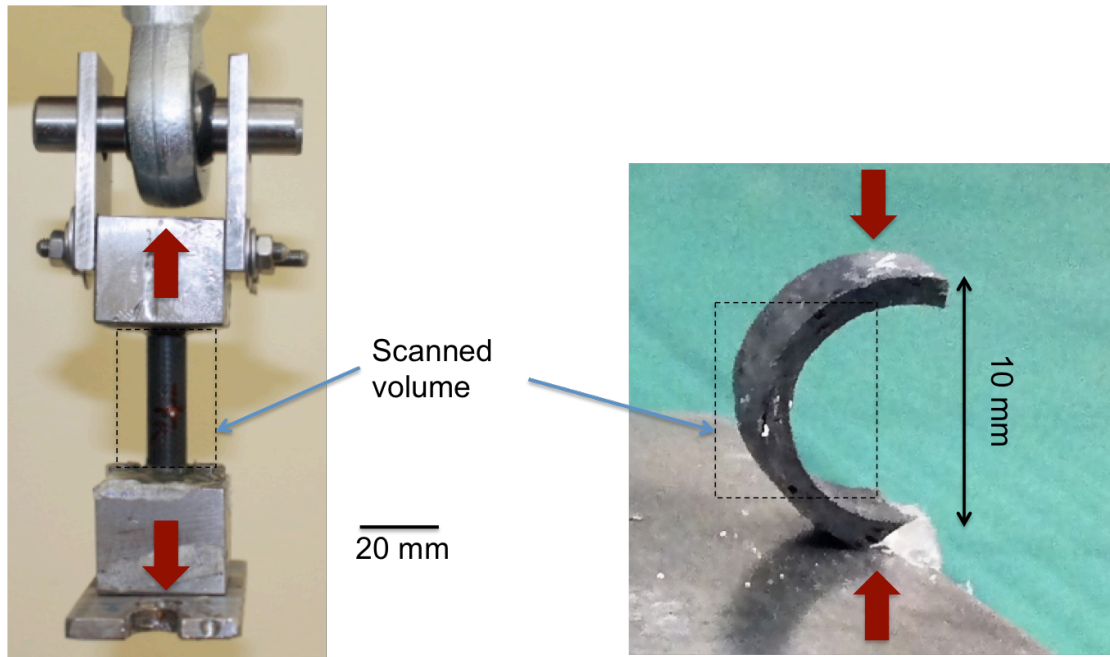


Figure 1: In situ testing of SiC-SiC specimens; a) the loading arrangements and imaged region for in situ tensile experiment at the Manchester X-ray Imaging Facility; b) the specimen, loading geometry and imaged region for in situ C-ring experiment at Diamond Light Source.

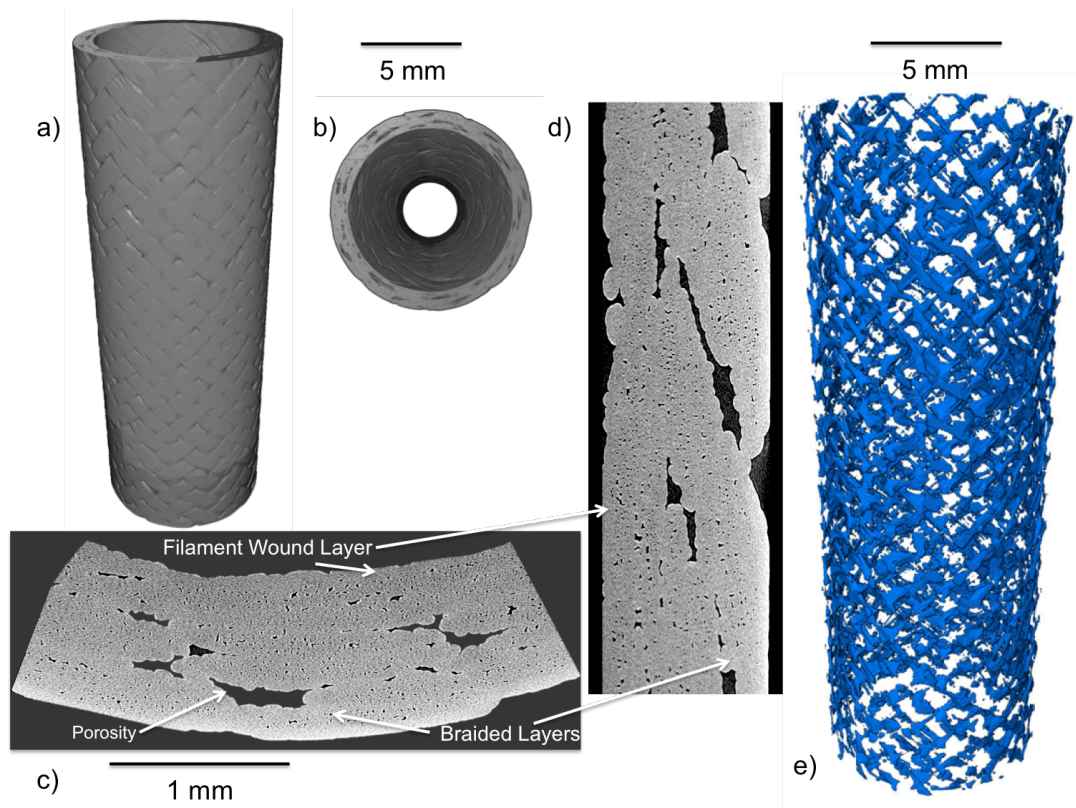


Figure 2: Visualization of the SiC-SiC composite tube microstructure; medium-resolution laboratory tomographs ($17\ \mu\text{m}$ voxel) as a) surface rendering and b) axial cross-section; compared with c) axial and d) longitudinal cross-sections of a high resolution tomograph ($1.7\ \mu\text{m}$ voxel). The porosity, segmented by image intensity thresholding from the medium-resolution tomograph, is shown in e).

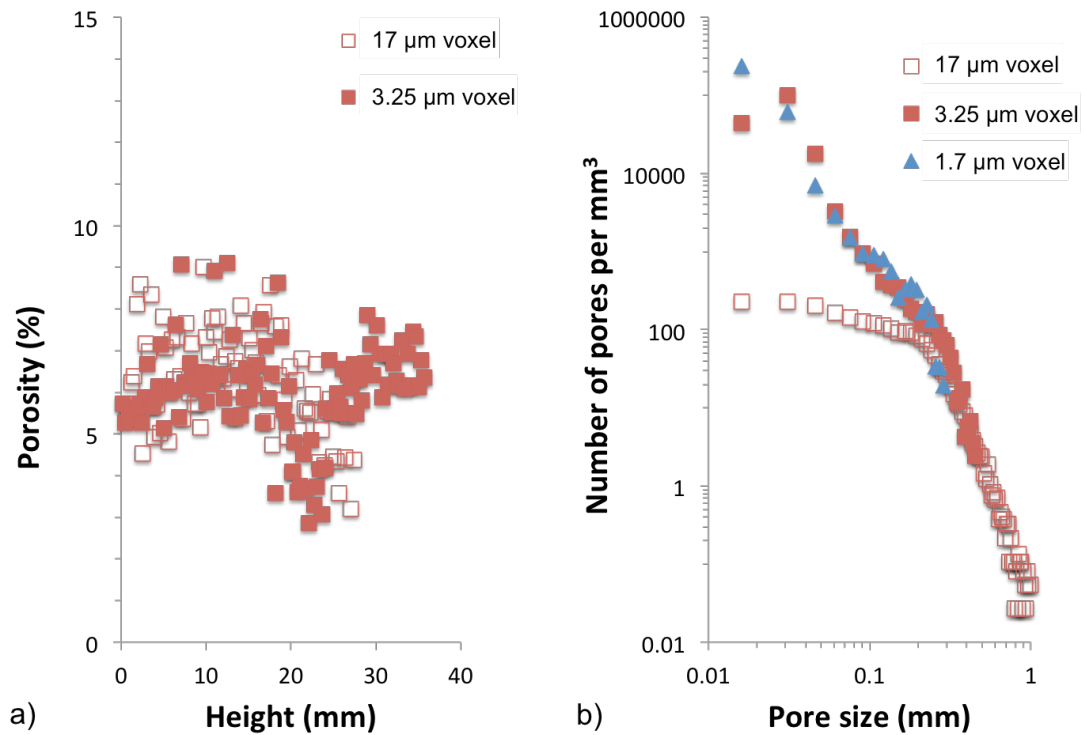


Figure 3: Quantitative analysis of detected porosity in two different specimens examined at different resolutions (i.e. voxel size): a) variation of total porosity with axial position (i.e. height); b) pore populations measured at different voxel resolutions. The 1.7 and 17 μm voxel data are from the same specimen. The representative volume dimensions are described in the text.

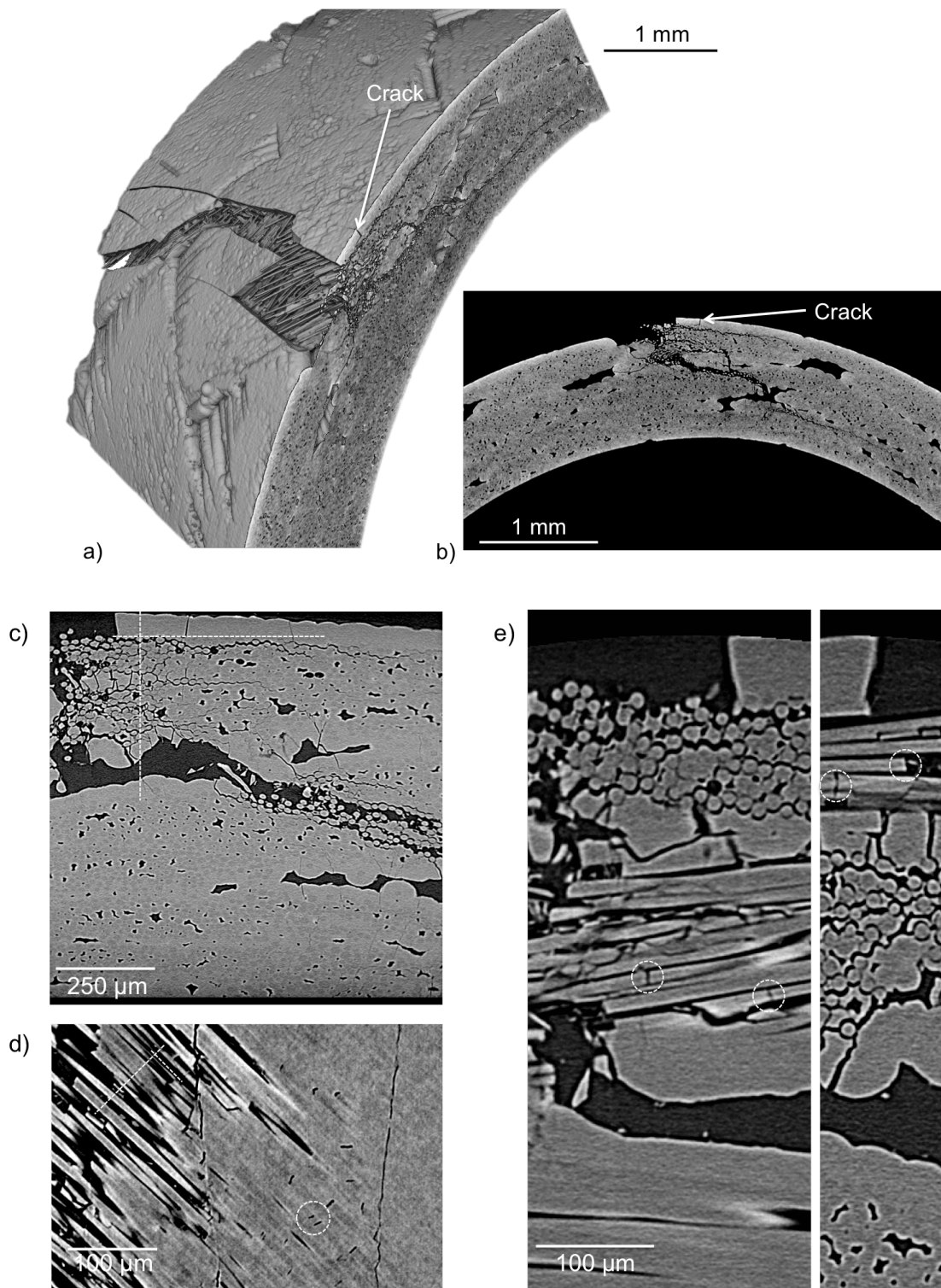


Figure 4: Post test X-ray tomography observations of C-ring: a) 3D surface rendering, cropped close to the centre of the sample to show damage and internal porosity – a crack in the monolithic layer is labelled; b) virtual slice of the X-ray attenuation data at the same position, in the plane of the tube circumference; c) higher resolution slice close to the same

This is the author's copy of a paper that was subsequently published in Journal of Nuclear Materials 481 (2016) pp13-23, <http://dx.doi.org/10.1016/j.jnucmat.2016.09.007>

plane; d) tangential slice ($1\ \mu\text{m}$ voxel) – the trace of the plane is marked in c); e) radial slices parallel and perpendicular to fibre tows – the traces of the slices are marked in c) and d). Broken fibres are circled in d) and e). The voxel size is $3.5\ \mu\text{m}$ in a) and b) and $1\ \mu\text{m}$ in c) to e).

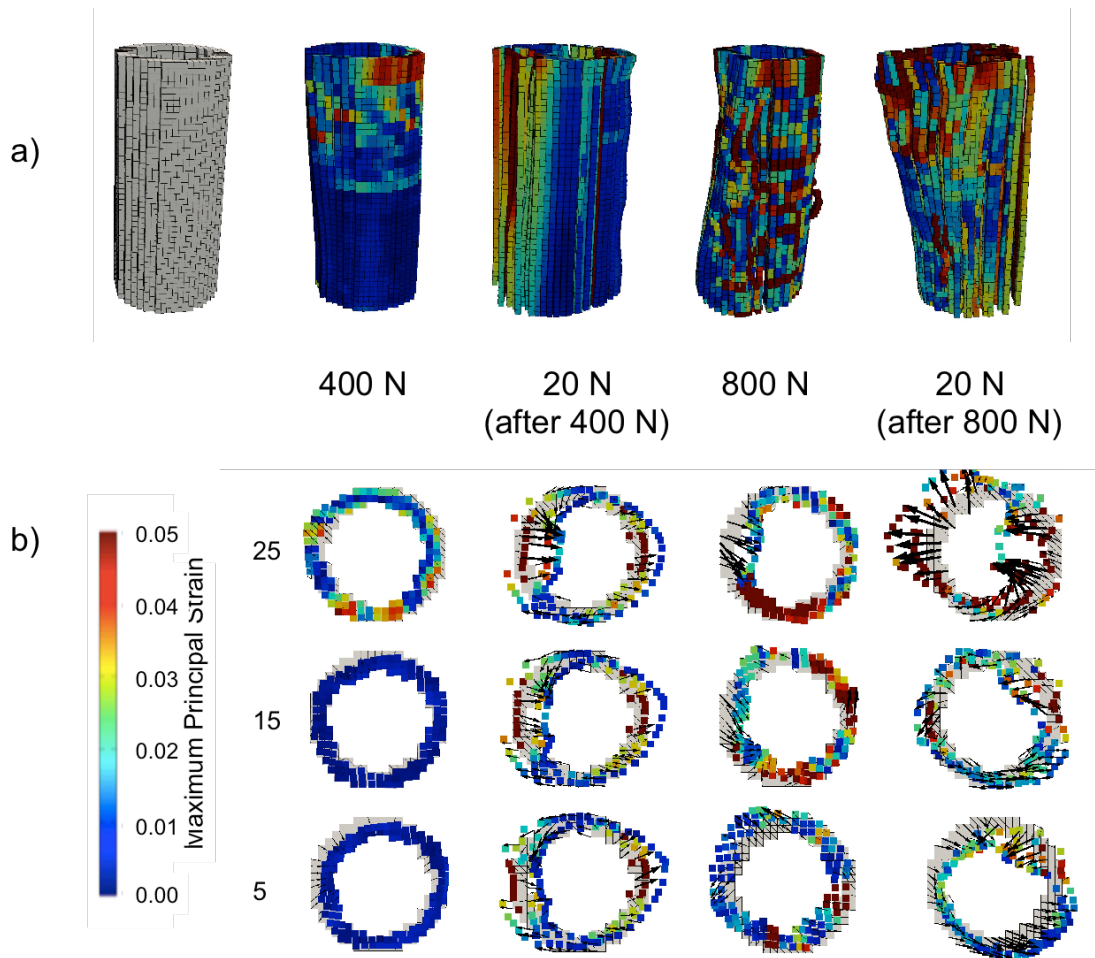


Figure 5: Deformation of the tensile loaded tube, with the magnitude of the maximum principal strain in the background. The displacements, measured by DVC of tomographs, are magnified and are relative to the average displacement of the specimen. Data are presented for the specimen in the loaded (400 N and 800 N) and unloaded (20 N) condition: a) visualisation of the whole analysed region of the specimen; b) example horizontal cross-sections of the displacement data at heights of 5, 15 and 25 mm (obtained in the horizontal plane).

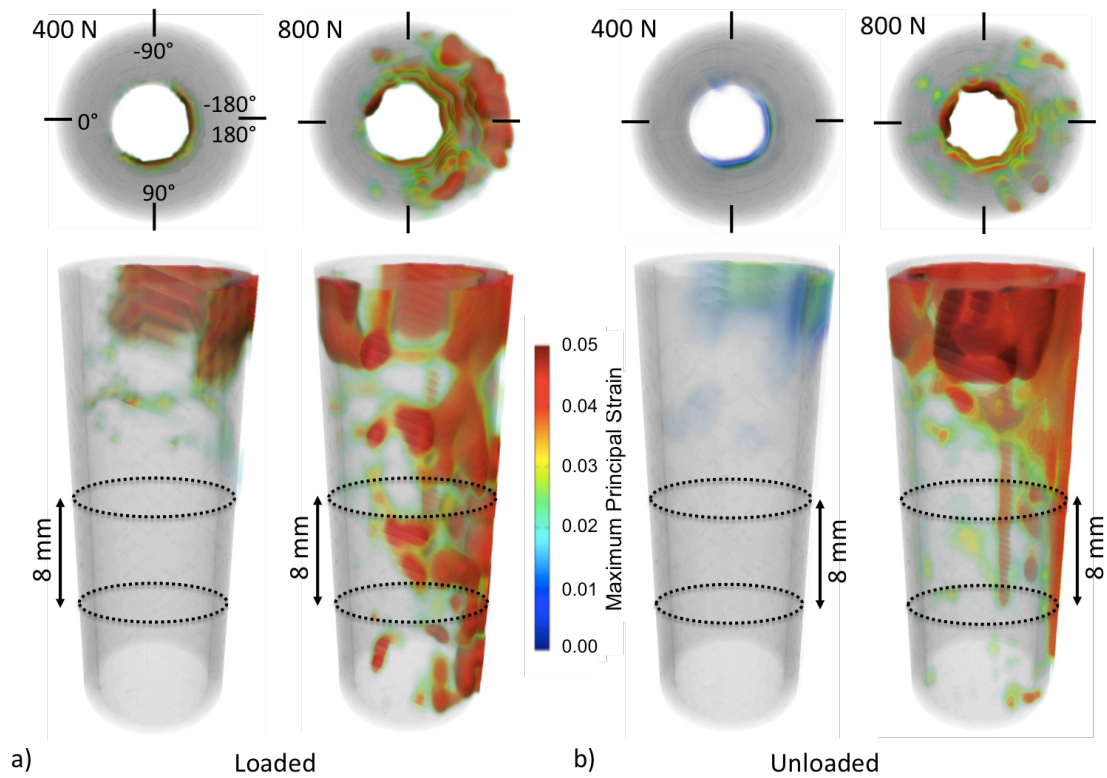


Figure 6: Visualisations, with perspective, of the maximum principal strain, obtained from the measured displacement fields of the tensile loaded tube (see Figure 5): a) under load at 400 N and 800 N; b) unloaded to 20 N after being loaded to 400 N and 800 N.

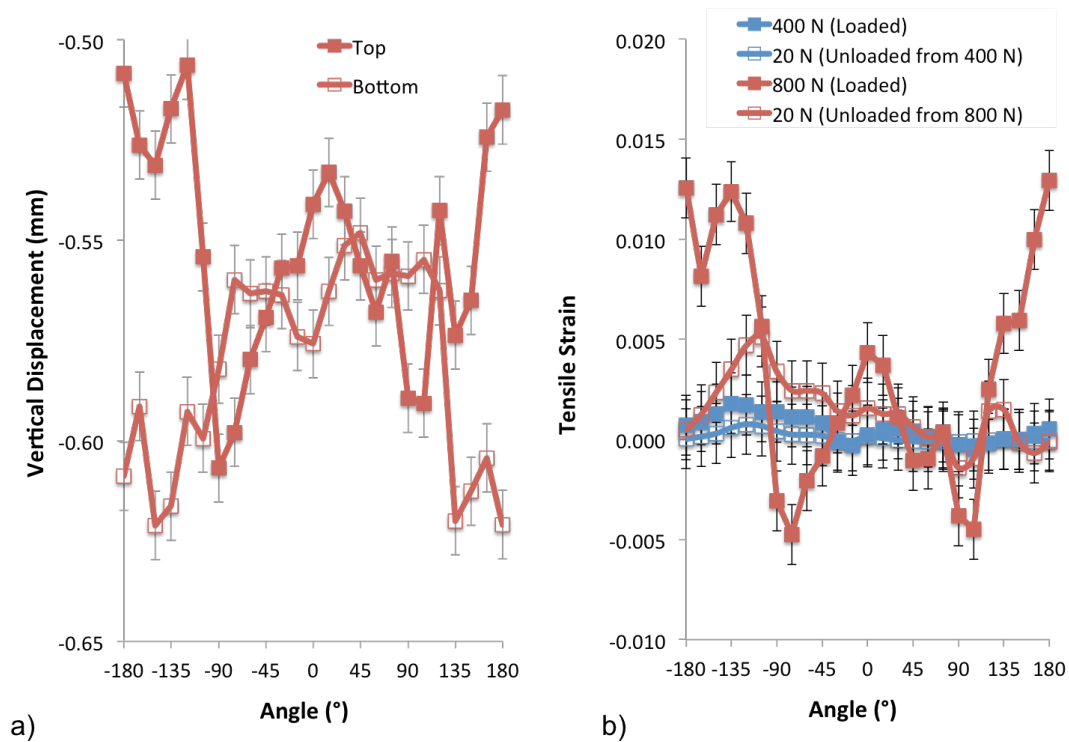


Figure 7: Measurement of the axial displacements and strains from the longitudinal displacement change around the circumference of the tensile loaded tube (see Figure 6); a) example vertical displacements at the top and bottom of the 8.2 mm gauge length at 800 N; b) axial strain in the loaded and unloaded states over the same gauge length. The error bars are calculated from an estimated displacement measurement uncertainty of 0.5 voxel (one voxel is 17 μm).

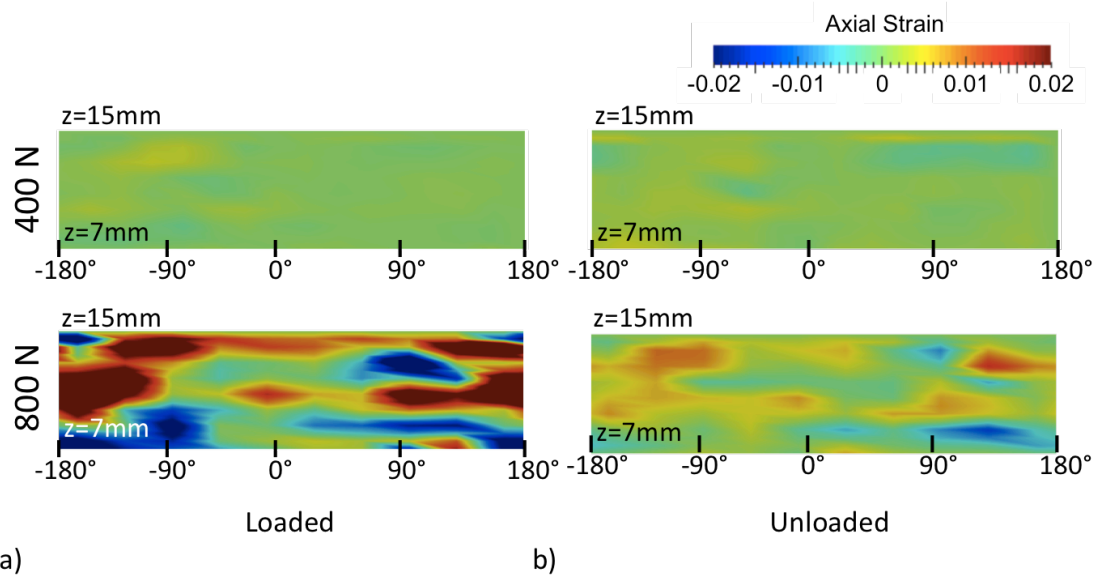


Figure 8: 2D visualisations of the axial strain in ~ 8 mm gauge length region of tensile loaded tube (see Figure 6: a) under load at 400 N and 800 N; b) unloaded to 20 N after being loaded to 400 N and 800 N.

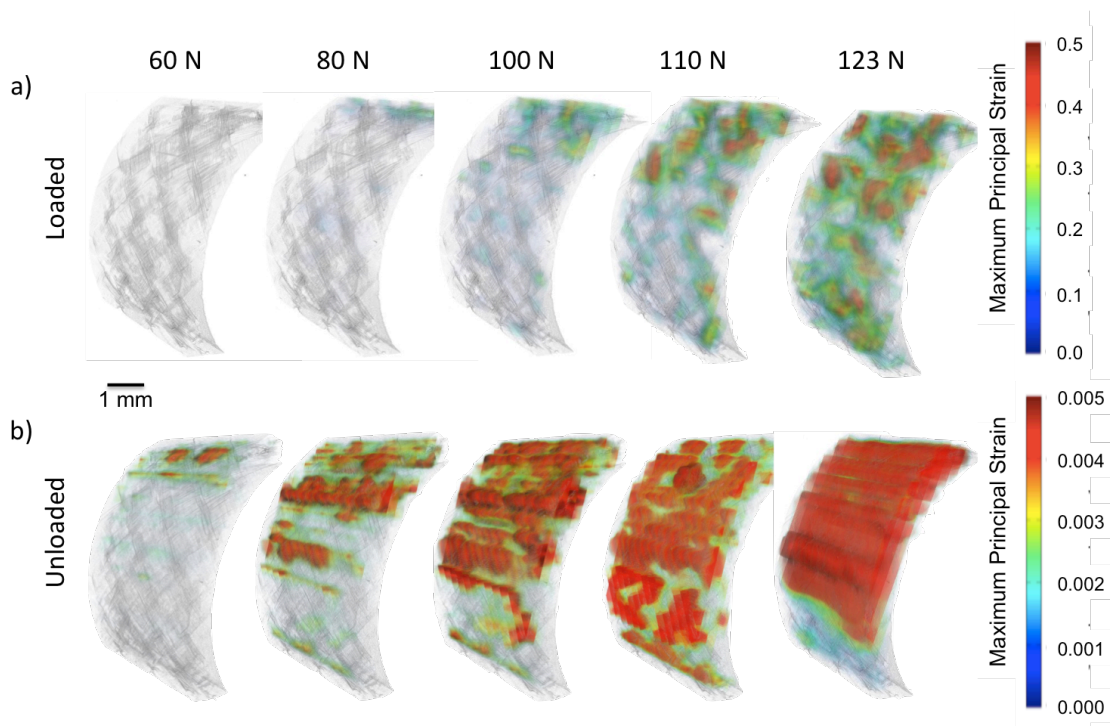


Figure 9: Visualisation of damage development in a section of the loaded and unloaded C-ring specimen as the maximum principal strains, calculated from the displacement field measured relative to the initial state before loading; a) loaded from 60 N to 123 N b) unloaded to ~ 5 N from peak loads of 60 N to 123 N.

This is the author's copy of a paper that was subsequently published in Journal of Nuclear Materials 481 (2016) pp13-23, <http://dx.doi.org/10.1016/j.jnucmat.2016.09.007>

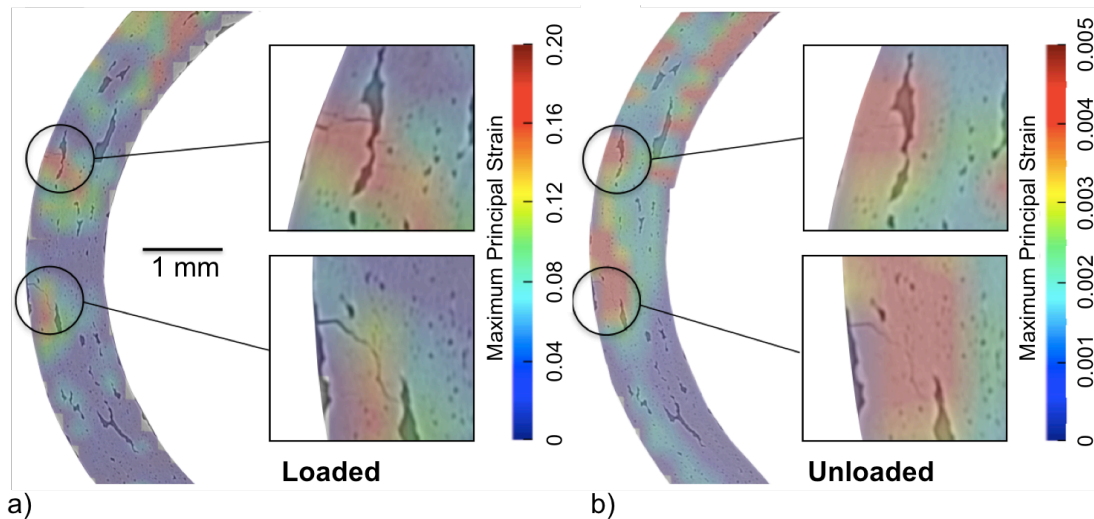


Figure 10: Example comparisons of the DVC-measured strain fields (i.e. Figure 9) with tomography observations of damage in the C-ring specimen when a) loaded (100 N) and b) unloaded (~5 N). The development of cracking at 2 locations is highlighted.

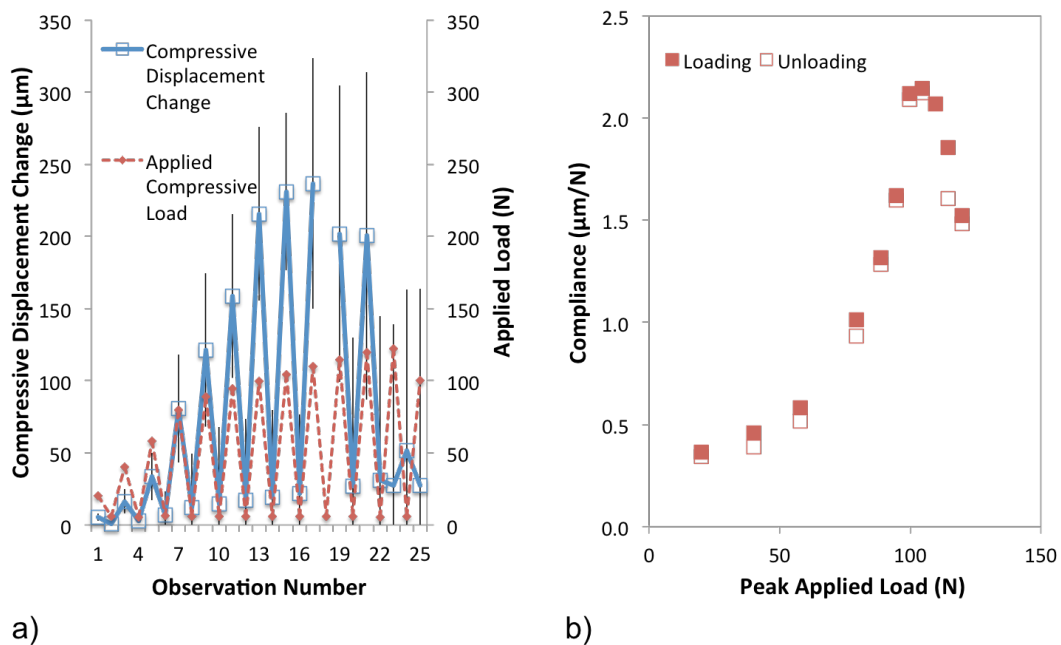


Figure 11: Load-displacement behaviour of the C-ring specimen: a) compressive displacement change measured over a central gauge of 5.4 mm as the applied load was progressively increased in cycles with intermediate unloads; b) the change in compliance with peak load, measured from the displacement change on loading and unloading.